

IMPLEMENTATION OF EARSM TURBULENCE MODEL WITHIN DISCONTINUOUS GALERKIN METHOD

A.I. Troshin*, V.V. Vlasenko*, A.V. Wolkov*
***Central Aerohydrodynamic Institute (TsAGI)**

Keywords: *discontinuous Galerkin method, turbulence model, accuracy order*

Abstract

A high-order discontinuous Galerkin method (DGM) is applied to the solution of 3D stationary RANS equations completed by the EARSM turbulence model. The method is implemented on unstructured hexahedral grids. The test problems are stationary and include flat-plate boundary layer, three element high-lift airfoil, and ONERA M6 wing. Mesh convergence is studied, accuracy orders acquired are evaluated, and conclusions concerning the applicability of DGM with a modern turbulence model to complex problems are made.

1 Introduction

Discontinuous Galerkin method (DGM) [1, 2] is one of the most perspective approaches to construct numerical schemes for solving aerodynamics problems. It combines the best properties of finite-volume (FV) methods (shock capturing and the possibility of taking into account the direction of information transport when approximating the fluxes at cells faces) and finite-element methods (weak dependence on the quality of the mesh used). An important feature of DGM is the possibility of constructing schemes of arbitrary high convergence order on a compact stencil consisting of just current cell and its nearest neighbors. It is relevant for practical problems with complex geometries which are being computed on large multiprocessor systems.

The problems of such scale often require adequate modeling of turbulence in different flow regions at the same time: in the vicinity of solid walls, in free shear regions, inside

separation zones, and in transients between them. Up to now, the most commonly used approach to turbulence modeling is still solving Reynolds system of equations completed by a semi-empirical turbulence model. In practice, two-equation linear eddy-viscosity models are used such as $k-\varepsilon$ [3] and SST [4]. Unfortunately, these models are often insufficiently general for consistent description of the effects appearing in computations. To some extent, these problems can be solved with the aid of turbulence models which do not rely on the Boussinesq hypothesis, particularly differential Reynolds stress models (DRSM) [5]. Such models offer advantages in many cases, but also possess significant drawbacks: high memory requirements and reduced computational stability. Due to these facts, DRSM models are still rarely used for solving the complex problems. In the last two decades, much effort is being made to develop compromise models requiring the solution of only two additional differential equations but employing more complex than Boussinesq formulas for Reynolds stresses [6, 7]. As compared to DRSM models, such models (which are called explicit algebraic Reynolds stress models – EARSM) use additional weak-equilibrium hypothesis which restricts their applicability to flows with high gradients of mean-flow quantities. However, they retain the possibility of describing the effects of turbulence anisotropy, streamline curvature and typically improve the separation modeling [7]. Nowadays, EARSM turbulence models are considered as one of the promising ways of increasing the accuracy of industrial level computations.

DGM applied to Reynolds system of equations is not still used in commercial CFD

programs as some issues related to stability, the need for limiters, mesh and polynomial adaptivity are yet unsolved. Such codes are being developed mainly by the academic community. Several turbulent solvers already exist which use linear eddy viscosity models [2] as well as EARSM [8]. In order to industrialize DGM, further investigation of its operation in conjunction with modern EARSM turbulence models is required. It is what the present paper is devoted to. In the paper, the numerical method is outlined for the complete compressible Reynolds system of equation closed with EARSM turbulence model based on [7], the features of its implementation based on the NUMECA Int. code Fine/OPEN™ [9] are described which is carried out within the European FP7 IDIHOM project (Industrialization of High-Order Methods, reference number 265780) as well as the results of the test computations. The test problems are stationary and include flat-plate boundary layer, three element high-lift airfoil, and ONERA M6 wing. Mesh convergence is studied, observed accuracy orders are evaluated, and conclusions concerning the applicability of DGM with a modern turbulence model to complex problems are made.

Among the features of the presented numerical method are: discontinuous Galerkin discretization in space with arbitrary shape functions order K (the tests were run with K up to 3) for all equations including those of turbulence model; first-order implicit scheme in time; adoption of hp multigrid strategy for the convergence acceleration to stationary solution; the use of BR2 method [10] to calculate the molecular and turbulent fluxes which depend on the gradients of the solution. To improve the computational stability, the equation for ω of the turbulence model [7] is rewritten in logarithmic form as recommended in [2], and for the turbulent kinetic energy k a limiter is introduced preventing it from taking negative values. An important element of the code is the use of soft relaxation which limits the increment of turbulent variables between the consequent time steps. Without these techniques, it would be impossible to obtain the results presented in the study.

2 Equation system and numerical method

The system of partial differential equations used in aerodynamics can be written in the following general form:

$$\Gamma \frac{\partial \mathbf{Q}}{\partial t} + \nabla \cdot \mathbf{F}(\mathbf{Q}, \mathbf{G}) = \mathbf{S}(\mathbf{Q}, \mathbf{G}), \quad (1)$$

where \mathbf{Q} is vector of primitive variables, Γ is matrix of transformation from \mathbf{Q} to vector of conservative variables \mathbf{U} , $\mathbf{G} = [\mathbf{G}_x; \mathbf{G}_y; \mathbf{G}_z]$ is vector of primitive variables gradients, \mathbf{S} is vector of conservative variables source terms. Vectors \mathbf{Q} , \mathbf{U} , \mathbf{G}_x , \mathbf{G}_y and \mathbf{G}_z have $N=7$ components. In our computations, $\mathbf{Q} = [\rho, u, v, w, p, k, \tilde{\omega}]$, $\mathbf{U} = [\rho, \rho u, \rho v, \rho w, \rho E, \rho k, \rho \tilde{\omega}]$, where $\tilde{\omega} = \ln \omega$, E is total energy per unit mass. We use a near-wall version of EARSM turbulence model [7] without blending function and “cross-diffusion” because the considered flows are characterized by the dominance of near-wall turbulence. Production limiter in $\tilde{\omega}$ equation is also dropped in order to increase the stability of computations.

A numerical solution of (1) in each cell of a computational grid is written as a linear combination of local polynomial shape functions $\varphi_j(\mathbf{x})$:

$$\mathbf{Q}(\mathbf{x}, t) = \sum_{j=1}^{K_f} q_j(t) \varphi_j(\mathbf{x}), \quad (2)$$

Coefficients $q_j(t)$ of expansion above are unknown values that have to be defined in DGM.

Representation of numerical solution in the form of (2) may be thought of as polynomial reconstruction of the gas parameters distribution within the computational cell. Theoretically, the DGM based on polynomials of the degree K should provide a solution of (1) with the accuracy order $(K+1)$.

To determine the dependence of q_j upon time, (1) is multiplied by φ_i and integrated over the cell volume Ω :

$$\int_{\Omega} \left(\Gamma \frac{\partial Q}{\partial t} + \nabla \cdot \mathbf{F}(Q, \mathbf{G}) \right) \varphi_i(\mathbf{x}) d\Omega = \int_{\Omega} \mathbf{S}(Q, \mathbf{G}) \varphi_i(\mathbf{x}) d\Omega. \quad (3)$$

Using the Gauss-Ostrogradsky formula, one can rewrite (3) as follows:

$$\int_{\Omega} \Gamma \frac{\partial Q}{\partial t} \varphi_i(\mathbf{x}) d\Omega + \oint_{\Sigma} \mathbf{F}_n \varphi_i(\mathbf{x}) d\Sigma = \int_{\Omega} \mathbf{F}_i d\Omega + \int_{\Omega} \mathbf{S} \varphi_i(\mathbf{x}) d\Omega, \quad (4)$$

where Σ is the cell surface, $\mathbf{F}_n = (\mathbf{F} \cdot \mathbf{n})$, \mathbf{n} is the outer unit normal to the surface element $d\Sigma$, and $\mathbf{F}_i = (\mathbf{F} \cdot \nabla \varphi_i(\mathbf{x}))$.

Convective flux terms in (4) are approximated according to Roe's approach [11]. Diffusive fluxes are computed using BR2 method [10]. For source terms, unconditionally stable scheme is used. It is based on eigenvalue analysis for Jacoby matrix $\partial \mathbf{S} / \partial Q$. If eigenvalue is negative, the point-implicit approximation is chosen for the corresponding part of source terms. Otherwise, this part is taken from the known time layer.

An implicit numerical method of first accuracy order in time is applied to obtain stationary solutions of (4). Let us introduce the increment operator for an arbitrary value b . This operator corresponds to transition from the time layer n to the time layer $(n+1)$: $\Delta b \equiv b^{n+1} - b^n$. The primitive variables Q^n at the time layer n are represented in the form of (2) with coefficients q_j^n , and the primitive variables at an arbitrary time t are represented as $Q(\mathbf{x}, t) = Q^n + \Delta Q(\mathbf{x}, t)$, where

$$\Delta Q(\mathbf{x}, t) = \sum_{j=1}^{K_f} \Delta q_j(t) \varphi_j(\mathbf{x}).$$

A time linearization of (4) is made giving a system of linear algebraic equations for Δq_j . For each cell c , let us denote the vector of unknowns

$$\overline{\Delta q}(c) \equiv \left((\Delta q_1)_{\rho}; (\Delta q_2)_{\rho}; \dots; (\Delta q_{K_f})_{\rho}; \dots; (\Delta q_1)_{\tilde{\omega}}; (\Delta q_2)_{\tilde{\omega}}; \dots; (\Delta q_{K_f})_{\tilde{\omega}} \right),$$

where K_f is shape functions number, and the vector of residuals

$$\overline{\mathbf{R}}(c) \equiv \left((\mathbf{R}_1)_{\rho}; (\mathbf{R}_2)_{\rho}; \dots; (\mathbf{R}_{K_f})_{\rho}; \dots; (\mathbf{R}_1)_{\tilde{\omega}}; (\mathbf{R}_2)_{\tilde{\omega}}; \dots; (\mathbf{R}_{K_f})_{\tilde{\omega}} \right).$$

With this notation, the system of equation reduces to the form

$$D(c) \overline{\Delta q}(c) + \sum_s H_s(c) \overline{\Delta q}(c_s(c)) = \overline{\mathbf{R}}(c), \quad (5)$$

where c is the current cell, $c_s(c)$ is the neighboring cell adjacent to the current cell c from the other side of the face s . $D(c)$ and $H_s(c)$ are square matrices of size $(K_f \cdot N) \times (K_f \cdot N)$ calculated from the solution at the time layer n .

The system (5) was solved by an iterative blockwise Jacoby method [12]. This method provides an acceptable convergence rate of iterations at low CPU and memory cost per iteration. The Gauss-Seidel method was also tested, but appeared to be unsuitable in conjunction with our implementation of DGM.

3 Test problems

3.1 Flat-plate boundary layer

The first test problem that demonstrates the performance of DGM is flat-plate turbulent boundary layer. The following freestream parameters are used: $V_{\infty} = 270$ m/s, $p_{\infty} = 101325$ Pa, $T_{\infty} = 300$ K, $k_{\infty} = 11$ m²/s², $\omega_{\infty} = 10^4$ Hz, which corresponds to $M_{\infty} \approx 0.78$, $Tu_{\infty} = \sqrt{2k_{\infty} / 3V_{\infty}^2} \times 100\% \approx 1\%$, $\mu_{t\infty} / \mu_{\infty} \approx 67$.

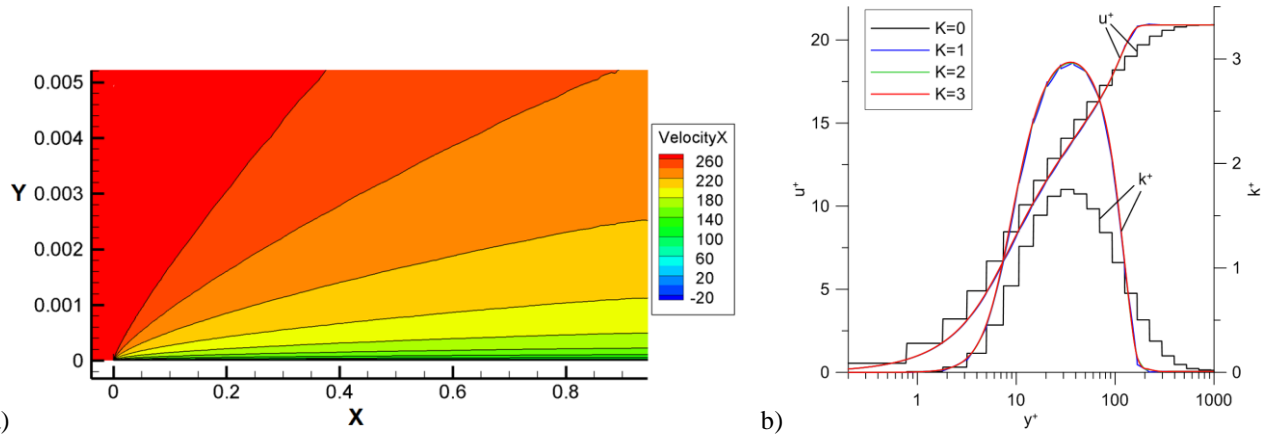


Fig. 1. a) flat-plate boundary layer velocity field, $K = 3$; b) dimensionless velocity and turbulent kinetic energy profiles for $x = 0.51 \text{ m}$ (corresponding to $\text{Re}_x \approx 1.6 \times 10^6$).

The computations are conducted on unstructured mesh consisting of 5185 quadrilateral cells. The plate is 1 m long. It is surrounded by computational domain with characteristic size 15 m in each direction. The height of the first cells above the plate is $h_y = 2 \times 10^{-6} \text{ m}$, which corresponds to $y^+ = y/l_\tau \approx 1$. Note that near a wall, length scale is

$$l_\tau = \sqrt{\nu_w \left| \frac{du}{dy} \right|_w},$$

and velocity scale is

$$u_\tau = \sqrt{\nu_w \cdot \left| \frac{du}{dy} \right|_w},$$

where variables with subscripts w are taken at the wall. The heights of the next cells above the wall are increased in geometric progression with geometric ratio 1.2. On both edges of the plate, x -axis refinement of the mesh is made with minimal cell size in x direction

$$h_x \approx 3.7 \times 10^{-4} \text{ m}.$$

The computations are run with maximal shape functions orders $K = 0, 1, 2, 3$. In each computation, variables distributions in $x = 0.747 \text{ m}$ section are obtained, which corresponds to length-based Reynolds number $\text{Re}_x = 1.8 \times 10^7$.

In Fig. 1, *a*, an overview of flat-plate boundary layer is presented. In Fig. 1, *b*, computed profiles $u^+(y^+) = u/u_\tau$ and $k^+(y^+) = k/u_\tau^2$ are shown. The van Driest transformation [13] was not used due to insignificant (within 0.15%) velocity profile changes for the selected flow regime. The solutions obtained with $K > 0$ almost coincide which indicates the polynomial convergence. In logarithmic region of the boundary layer ($u^+ = (\ln y^+)/\kappa + B$), the following values of constants are determined from the computations: $\kappa = 0.40$, $B = 4.4$. They satisfactory match the empirical values $\kappa_{\text{exp}} = 0.4$, $B_{\text{exp}} = 5$.

Table 1. Grid sizes and characteristic spacings for three-element airfoil.

Grid ID #	number of cells	height of the first near-wall cell (m)	increment of cell size growth	max. nbr. layers
1	2 836	8.9×10^{-5}	2.14	4
2	7 432	3.7×10^{-5}	1.46	8
3	20 854	1.7×10^{-5}	1.21	10
4	102 108	1.0×10^{-5}	1.20	30
5	168 677	5.0×10^{-7}	1.20	50
6	308 966	5.0×10^{-7}	1.20	50

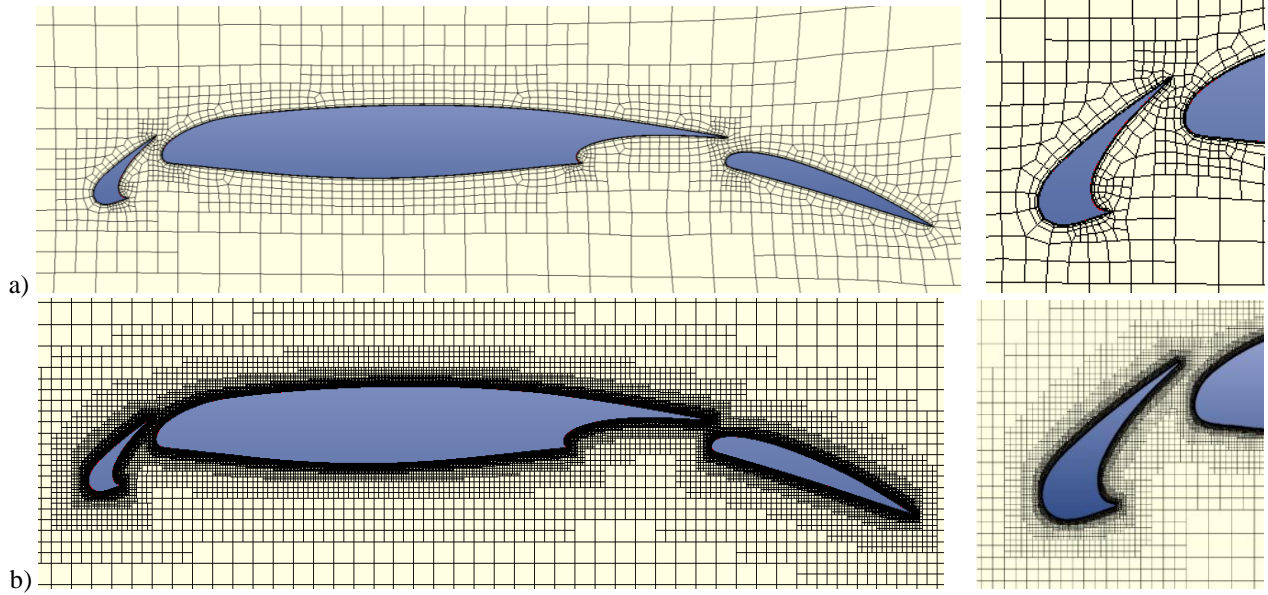


Fig. 2. Unstructured coarse (a) and fine (b) grids: overall view of the airfoil (left) and details at the slat (right).

3.2 Subsonic flow around a three-element airfoil

Implicit DGM solver for RANS equations has been applied to the computation of subsonic flow around a three-element airfoil L1T2 [14] at the Mach number $M_\infty = 0.197$, the angle of attack $\alpha = 20.18^\circ$, the chord-based Reynolds number $Re = 3.52 \times 10^6$. Turbulence parameters of the ambient flow are $k_\infty = 0.68 \text{ m}^2/\text{s}^2$ ($Tu_\infty = 1.0\%$), $\omega_\infty = 4.5 \times 10^4 \text{ Hz}$ (which gives $\mu_{t_\infty} \approx \mu_\infty$).

Two sequences of unstructured purely hexahedral hanging node grids have been generated with the industrial grid generator HEXPRESS by NUMECA (see Table 1). The first one (#1, #2, and #3) is used for computations with a high-order DGM, while the

performance of FV method was studied on finer #4, #5 and #6 grids. The Fig. 2 visualizes the fragments of the coarsest and the finest grids with 2 836 and 308 966 elements, respectively. While the refinement can be seen, it is also clear that these three grids do not constitute a nested hierarchy of grids.

The outer boundary of the computational domain is placed at the distance of 10 chords from the airfoil, and boundary condition at this boundary is based on analysis of Riemann invariants. To take into account the velocity circulation, additional velocity field $\vec{V}_\Gamma(\vec{r})$ is superimposed at the boundary point \vec{r} :

$$\vec{V}_\Gamma(\vec{r}) = \frac{\Gamma \vec{\tau}}{2\pi |\vec{r} - \vec{r}_c|},$$

where \vec{r}_c is the central point of the airfoil, $\vec{\tau}$ is

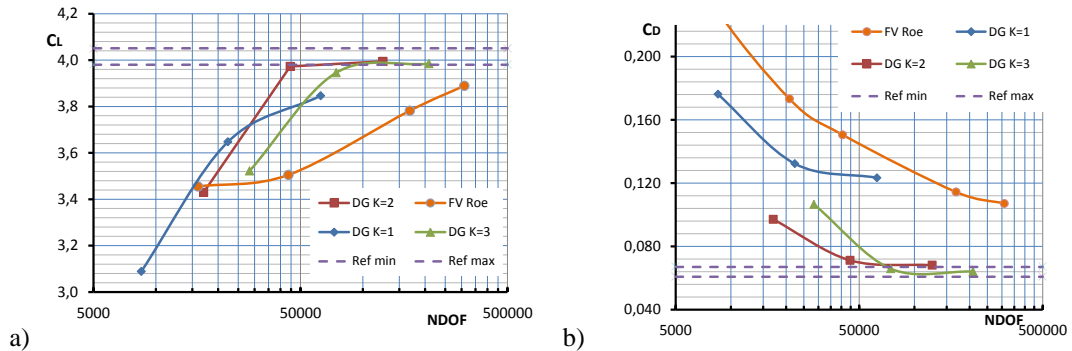


Fig. 3. a) C_L and b) C_D characteristics of L1T2 three-element airfoil for different numerical schemes vs. NDOF.

Table 2. Extrapolation of asymptotic reference values for the lift coefficient C_L^* .

K	<i>using two grids</i>		<i>using three grids</i>	
	theoretical order	asymptotic value	observed order	asymptotic value
1	2	3.956	2.2	3.939
2	3	4.000	6.7	3.995
3	4	3.990	5.0	3.988

Table 3. Extrapolation of asymptotic reference values for the drag coefficient C_D^* .

K	<i>using two grids</i>		<i>using three grids</i>	
	theoretical order	asymptotic value	observed order	asymptotic value
1	2	0.1185	3.4	0.1215
2	3	0.0673	4.4	0.0678
3	4	0.0638	6.5	0.0640

unit vector normal to $\vec{r} - \vec{r}_c$, and Γ is the prescribed circulation value. Solid surfaces are treated as adiabatic no-slip walls.

In high-order DGM computations ($K = 2$ and 3), the curvature of grid lines in the vicinity of solid surfaces has been taken into account, cell edges being considered as elements of parabolas.

To achieve fully-2D computation, 2D shape functions have been used. Computations were performed with local time stepping. Each computation started from local Courant number $CFL = 1$. If a flow field computed in the current iteration was physical, the CFL was incremented 1.5 times. Otherwise, the numerical solution was returned to the state before the iteration, and the iteration was repeated with 2–10 times smaller value of the CFL. In all computations, the maximal value of CFL was restricted by $CFL=1000$, except for the $K = 3$ computation on the #3 grid, where the CFL was restricted as $CFL=100$. In all computations, deep convergence to stationary flow has been achieved (residual has decreased by 8–15 orders of magnitude from the initial level). Computations have been parallelized, up to 48 processor cores were used. In Fig. 3, integral characteristics of considered three-element airfoil are shown for different numerical schemes (DGM $K = 1$, $K = 2$, and FV) versus number of degrees of freedom (NDOF). The FV method used is implemented in the industrial

FINE/Open™ (NUMECA Int.) code. This is a second order Roe upwind scheme. The range of asymptotic reference values obtained by different numerical methods on a sequence of grids [15] is also depicted. The reference lift coefficient C_L varied from 3.98 to 4.05 and the drag coefficient C_D varied from 0.0608 to 0.0670.

Note that the considered FV approach is obviously inferior to high-order DGM ($K = 2, 3$) and even $K = 1$. In case of DGM, monotonic variation of lift and drag coefficients with increasing the number of grid cells allowed us to calculate the asymptotic values by two approaches. In the first approach, assuming a theoretical order of accuracy we are able to estimate the asymptotic value of C_L and C_D based on the computations on two grids. The second approach uses C_L and C_D values on three successive grids which allow us to evaluate not only the asymptotic value on the infinitely fine grid, but also the observed order of accuracy. The results of both approaches are presented in Tables 2 and 3. Note that the asymptotic values obtained in different schemes are quite close to each other, that reflects the high quality of the obtained solutions. However, evaluated accuracy orders of DGM are unrealistically high. This can be explained by the fact that employed grid sequence is not fully nested. Nevertheless, the good agreement

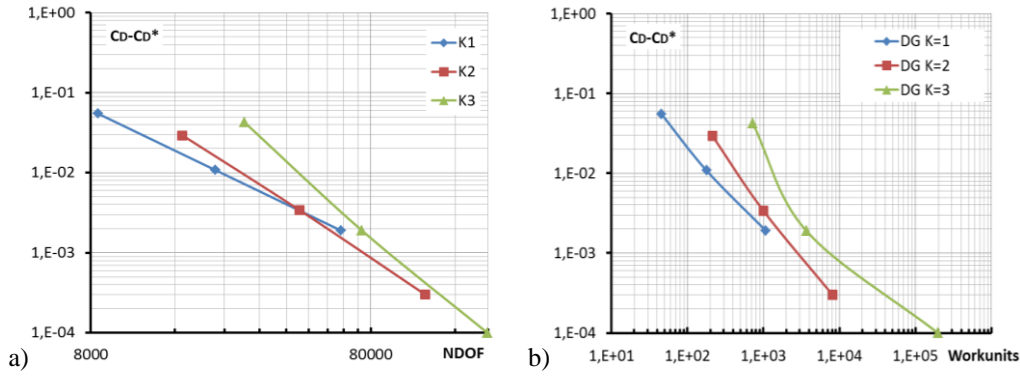


Figure 4. C_D error for different schemes vs. a) NDOF and b) normalized run-time.

between results indicates that the grid sequence is well suited for this test case.

The Fig. 4, *a* presents the C_D error on the logarithmic scale for schemes with different K versus NDOF. In accordance with the theoretical prediction, the slope of lines varies depending on the scheme order. Thus, in practice, the choice of the scheme order should be defined by the desired degree of accuracy. As can be seen in Fig. 4, *b*, the third-order method (DGM $K=2$) is preferable for C_D with error less than 10^{-3} . Unfortunately, the practical implementation of the fourth-order method (DGM $K=3$) was too costly and slow compared with DGM $K=2$. The quadrature formulas are probably to be revised.

Efficiency of high-order computations compared to the conventional second-order FV scheme is also illustrated by Fig. 5, where results on different grids are presented versus normalized run-time. Here one can see that

convergence to values of coefficient C_D to reference values is achieved much more quickly with $K=2, 3$ compared to second-order DGM $K=1$ and industrial FV FINE/Open™ code.

3.2 Transonic flow around isolated wing

Computations of transonic flow around the wing ONERA M6 have been performed for the following flow regime (TEST 2308 from [16]): the Mach number $M_\infty = 0.8395$, the angle of attack $\alpha = 3.06^\circ$, the mean aerodynamic chord-based Reynolds number $Re = 11.72 \times 10^6$, and the stagnation temperature $T_0 = 300 K$. Turbulence parameters of the ambient flow are $k_\infty = 10 \text{ m}^2/\text{s}^2$ ($Tu_\infty \approx 1\%$) and $\omega_\infty = 6.7 \times 10^5 \text{ Hz}$ (which gives $\mu_{t_\infty} \approx \mu_\infty$).

Three subsequent unstructured hexahedral grids have been generated. Their characteristics are presented in Table 4. Fragments of grids on the wing surface are shown in Fig. 6.

Table 4. Grid sizes and characteristic spacings

Grid ID	nbr. cells	height of the first near-wall cell (m)	increment of cell size growth	Max. nbr. layers
1 (Coarse)	38219	3.0×10^{-4}	4.0	5
2 (Med.)	75987	1.5×10^{-4}	3.5	7
3 (Fine)	204062	7.5×10^{-5}	2.0	10

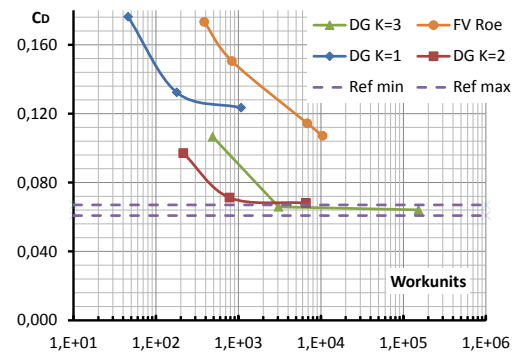


Fig. 5. Grid convergence as a function of normalized run-time.

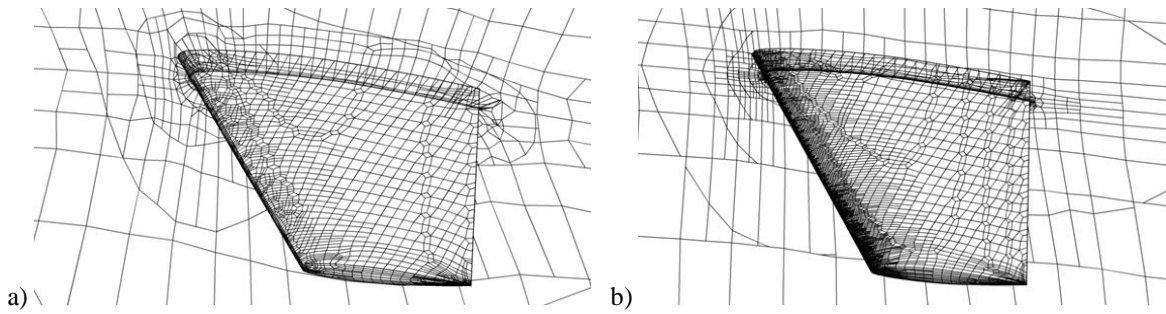


Fig. 6. Unstructured grids around ONERA M6 wing: a) coarse and b) fine.

In the vicinity of solid surfaces, curvature of grid lines has been taken into account in DGM $K=2$ computations. We were unable to achieve convergence with a fourth-order numerical scheme, which is possibly due to the lack of a special shock capturing procedure.

Wing pressure distributions C_p obtained on different grids in the middle section $x/c = 0.65$ is presented in Fig. 7. It can be seen from the figure that the solution converges to the experimental curve when the grid is refined. The convergence rate is approximately the same for both DGM $K=1$ and DGM $K=2$.

In Fig. 8, the plots of C_L and C_D versus NDOF are presented. It is seen that asymptotic values of DGM $K=1$ and DGM $K=2$ are

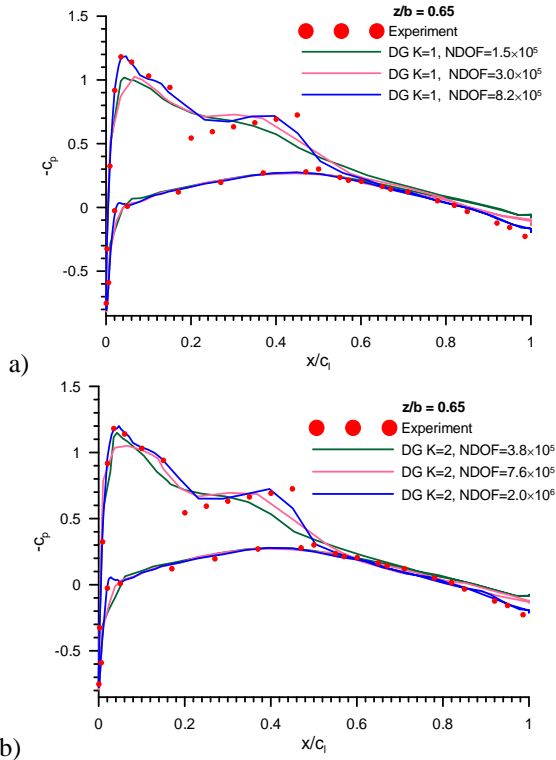


Fig. 7. Pressure distributions for different grid densities: DGM a) $K=1$ and b) $K=2$.

different. Assuming a monotone grid convergence, an estimation based on three points gives the following asymptotic values: for DGM $K=1$, $C_L^* = 0.2825$, $C_D^* = 0.0149$; for DGM $K=2$, $C_L^* = 0.2746$, $C_D^* = 0.0126$.

Such a difference is probably explained by the presence of shock wave even on the coarsest grid. It is known that such singularities do not allow obtaining the approximate solution with an accuracy order higher than 1. Achieving good-quality solutions is only possible on grids with highly refined cells near shocks. Employment of high-order schemes in shock regions is not justified and requires artificial elimination of nonphysical solution oscillations. From the computational resource viewpoint, the use of high-order schemes can be efficient in smooth regions. That should be combined with grid refinement in the shock regions and applying the special monotonicity procedures [17].

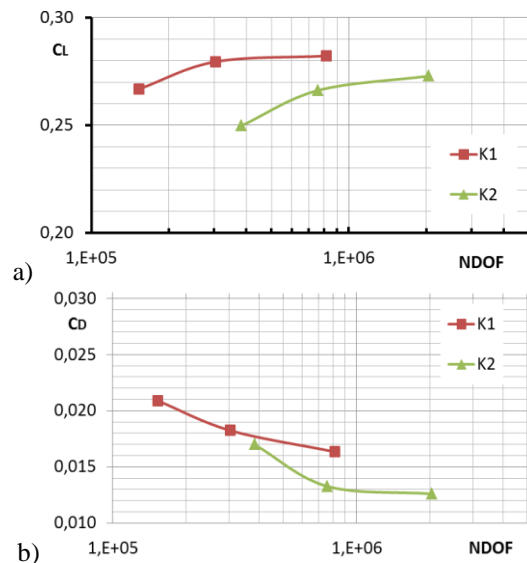


Fig. 8. a) C_L and b) C_D characteristics of ONERA M6 wing vs. NDOF for DGM $K=1$ and 2.

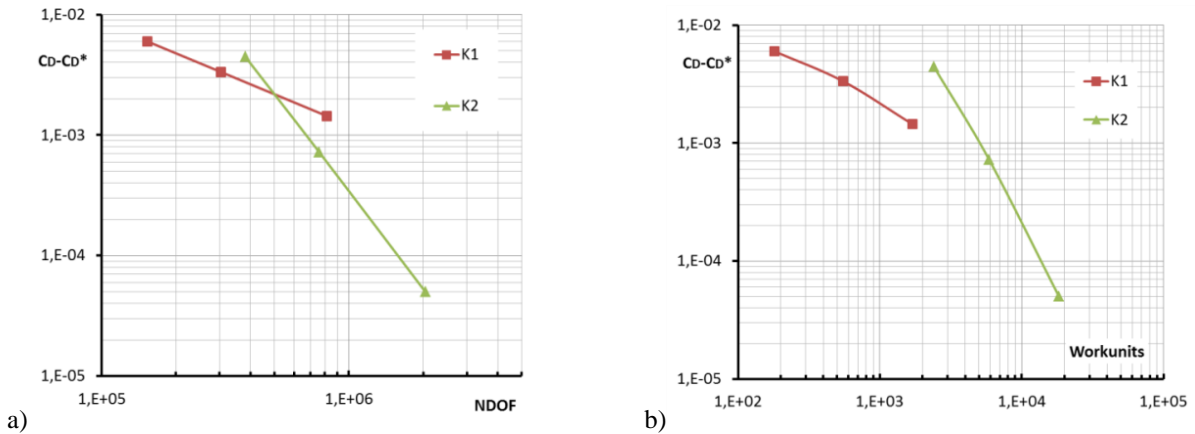


Fig. 9. C_D error for different schemes vs. a) NDOF and b) normalized run-time.

In accordance with the theory, the slope of C_D error versus NDOF lines (Fig. 9, a) for DGM $K = 2$ is higher than for DGM $K = 1$, but individual choice of the scheme should be done with regard to run-time and required accuracy. Thus, as follows from Fig. 9, b, the advantage of using higher-order schemes will be apparent if one needs the precision of C_D better than 10^{-4} .

4 Conclusions

High-order discontinuous Galerkin method was implemented within the industrial second-order finite volume code FINE/Open™ developed by NUMECA Int. based on unstructured hexahedral grids generated by HEXPRESS™. The full system of RANS equations completed by an EARSM class turbulence model was approximated by high-order spatial discretization up to the order 4 and an implicit temporal smoother of first accuracy order in time was used for the solution. Subsonic and transonic problems of external aerodynamics were considered.

The main expected advantage of using high-order methods is the possibility to get the same quality of results on much coarser grids and at substantially lower computational cost. This advantage was demonstrated for subsonic high-lift test cases. Profit is most evident in the case of determining the drag coefficient. Second-order accuracy schemes demonstrated significantly slower grid convergence.

In the case of problems with shock waves (transonic flow over the ONERA M6 wing),

obvious profit was not obtained. Shock waves resolution requires local grid refinement and/or employment of special shock capturing procedures. The use of high accuracy order numerical schemes could be helpful if precise determination of the drag coefficient were required.

Acknowledgments

We gratefully acknowledge funding of this work under the target research project IDIHOM (2010-2014) of 7th European Research framework program.

We gratefully acknowledge the President of NUMECA Charles Hirsch for providing industrial code FINE/Open™ and cooperation in performing of the present research.

We gratefully acknowledge the project manager, deputy chief of TsAGI Sergey Bosnyakov for his huge work on the coordination of our efforts.

We gratefully acknowledge the junior researcher of TsAGI Igor Bosnyakov for his numerous calculations of various test cases.

References

- [1] Wang Z.J. High-order methods for the Euler and Navier–Stokes equations on unstructured grids. *Progress in Aerospace Sciences*, Vol. 43, pp 1-41, 2007.
- [2] Bassi F., Crivellini A., Rebay S. and Savini M.. Discontinuous Galerkin solution of the Reynolds-averaged Navier–Stokes and $k-\omega$ turbulence model

- equations. *Computers & Fluids*, Vol. 34, pp 507-540, 2005.
- [3] Launder B.E. and Sharma B.I. Application of the energy dissipation model of turbulence to the calculation of flow near a spinning disc. *Letters in Heat and Mass Transfer*, Vol. 1, No. 2, pp 131-138, 1974.
- [4] Menter F.R. Two-equation eddy-viscosity turbulence models for engineering applications. *AIAA Journal*, Vol. 32, No. 8, pp 1598-1605, 1994.
- [5] Hanjalić K. Second-moment turbulence closures for CFD: needs and prospects. *International Journal of Computational Fluid Dynamics*, Vol. 12, pp 67-97, 1999.
- [6] Hellsten A. New advanced $k-\omega$ turbulence model for high-lift aerodynamics. *AIAA Journal*, Vol. 43, No. 9, pp 1857-1869, 2005.
- [7] Menter F.R., Garbaruk A.V. and Egorov Y. Explicit algebraic Reynolds stress models for anisotropic wall-bounded flows. *Proc 3rd European Conference for Aero-Space Sciences*, Versailles, 14 p, 2009.
- [8] Bassi F., Botti L., Colombo A. and De Bartolo C. Implicit high-order discontinuous Galerkin solution of turbulent flows with an explicit algebraic Reynolds stress model. *Proc 6th European Congress on Computational Methods in Applied Sciences and Engineering*, Vienna, 16 p, 2012.
- [9] www.numeca.be.
- [10] Bassi F., Rebay S., Mariotti G., Pedinotti S. and Savini M. A high-order accurate discontinuous finite element method for inviscid and viscous turbomachinery flows. *Proc 2nd European Conference on Turbomachinery – Fluid Dynamics and Thermodynamics*, Antwerpen, pp 99-108, 1997.
- [11] Roe P.L. Approximate Riemann solvers, parameter vectors, and difference schemes. *Journal of Computational Physics*, Vol. 43, No. 2, pp 357-372, 1981.
- [12] Ortega J.M. *Introduction to parallel and vector solution of linear systems*. Plenum Press, 1988.
- [13] White F.M. *Viscous fluid flow*. 3rd edition, McGraw-Hill, 2006.
- [14] Moir I.R.M. Measurements on a two-dimensional aerofoil with high-lift devices. *A Selection of Experimental Test Cases for the Validation of CFD Codes*, ed. by M. Burt, NATO, Neuilly-Sur-Seine, France, chap. A/2, 1994.
- [15] Leicht T. Test case final summary report.U.3 L1T2 high lift airfoil. Results of the project IDIHOM (2010-2014) of 7th European Research framework program. To be published.
- [16] Schmitt V. and Charpin F. Pressure distribution on the ONERA M6 wing at transonic Mach numbers. *AGARD AR-138 report*, Office National D'étude et de Recherches Aérospatiales, Chatillon, France, 1979.
- [17] Barter G.E. and Darmofal D.L.. Shock capturing with PDE-based artificial viscosity for DGFEM: Part I. Formulation. *Journal of Computational Physics*, Vol. 229, No. 5, pp 1810-1827, 2010.

Contact Author Email Address

mailto: andrey.wolkov@tsagi.ru

Copyright Statement

The authors confirm that they, and/or their company or organization, hold copyright on all of the original material included in this paper. The authors also confirm that they have obtained permission, from the copyright holder of any third party material included in this paper, to publish it as part of their paper. The authors confirm that they give permission, or have obtained permission from the copyright holder of this paper, for the publication and distribution of this paper as part of the ICAS 2014 proceedings or as individual off-prints from the proceedings.